



Article

Influence of Stabilizing Ion Content on the Structure, Photoluminescence and Biological Properties of $Zr_{1-x}Eu_xO_{2-0.5x}$ Nanoparticles

Alexander N. Bugrov ^{1,2,*}, Ruslan Yu. Smyslov ^{2,3} , Anastasia Yu. Zavialova ¹,
Gennady P. Kopitsa ^{3,4}, Tamara V. Khamova ⁴, Demid A. Kirilenko ⁵, Ilya E. Kolesnikov ⁶,
Dmitrii V. Pankin ⁶, Vadim A. Baigildin ⁶  and Christophe Licitra ⁷

¹ Saint Petersburg Electrotechnical University “LETI,” ul. Professora Popova 5, St. Petersburg 197376, Russia; aizavialova@etu.ru

² Institute of Macromolecular Compounds, Russian Academy of Sciences, Bolshoy pr. 31, St. Petersburg 199004, Russia; urs@macro.ru

³ Petersburg Nuclear Physics Institute, Orlova roscha mcr. 1, Gatchina 188300, Leningrad region, Russia; kopitsa_gp@pnpi.rncki.ru

⁴ Grebenshchikov Institute of Silicate Chemistry R.A.S., Makarova nab. 2., letter B, St Petersburg 199034, Russia; tamarakhamova@gmail.com

⁵ Ioffe Institute, Politekhnikeskaya 26, St. Petersburg 194021, Russia; demid.kirilenko@mail.ioffe.ru

⁶ Resource Center for Optical and Laser Materials Research, St. Petersburg State University, St. Petersburg 199034, Russia; ilya.kolesnikov@spbu.ru (I.E.K.); dmitrii.pankin@spbu.ru (D.V.P.); st804289@spbu.ru (V.A.B.)

⁷ University Grenoble Alpes, CEA, LETI, F-38000 Grenoble, France; christophe.licitra@cea.fr

* Correspondence: anbugrov@etu.ru; Tel.: +7-812-323-6269

Received: 15 October 2020; Accepted: 9 November 2020; Published: 15 November 2020



Abstract: Quasi-spherical nanoparticles of ZrO_2 containing $EuO_{1.5}$ from 2 to 15 mol.% were synthesized from the chlorides of the corresponding metals under hydrothermal conditions. The structural changes of $Zr_{1-x}Eu_xO_{2-0.5x}$ ($x = 0.02 \div 0.15$) nanoparticles depending on the content of europium (III) ions were studied using the complementary methods (X-ray diffraction, electron microdiffraction, Raman and photoluminescence spectroscopy). It was shown that increasing the Eu^{3+} concentration in the $Zr_{1-x}Eu_xO_{2-0.5x}$ nanoparticles leads to a transition from the equilibrium monoclinic zirconia phase to metastable tetragonal and cubic polymorphic modifications. In this case, the size of the nanoparticles decreases from 11.5 nm to 9 nm; the specific surface area grows from 80.2 to 111.3 m^2/g , and the electrokinetic potential increases monotonously from -8.7 to 16.3 mV. The evolution of the phase composition of $Zr_{1-x}Eu_xO_{2-0.5x}$ nanoparticles from monoclinic to tetragonal/cubic allomorphs with an increase in the molar fraction of stabilizer ions was correlated with changes in the sublevel structure of $^5D_0 \rightarrow ^7F_2$ and $^5D_0 \rightarrow ^7F_4$ optical transitions for Eu^{3+} in the luminescence spectra. Besides, for the nanoparticles obtained by hydrothermal synthesis from chlorides, the quantum efficiency does not exceed 3%. According to the M.T.T. assay, as a result of three-day human fibroblast cultivation in the aqueous dispersion of $Zr_{1-x}Eu_xO_{2-0.5x}$ ($x = 0.02 \div 0.15$) nanoparticles, the proliferation activity of the cells is maintained, indicating that they do not have cytotoxic properties. Such nanoparticles can be used in organic–inorganic composites for medical applications in order to strengthen the polymer scaffolds and visualize changes in their structure within time.

Keywords: hydrothermal synthesis; zirconia; rare-earth ions; phase composition; photoluminescence; cytotoxicity

1. Introduction

Recently, more and more attention has been paid to the development of highly sensitive and safe nanophosphors for probing and visualizing biological objects [1–3]. Inorganic nanoparticles doped with lanthanide ions (Ln^{3+}) for use in biomedical applications should be biocompatible, exhibit intense luminescence and low toxicity, and have good colloidal stability in water and biological solutions [4,5]. In addition, small diameter nanoparticles with a narrow size distribution are required, which can be easily functionalized using surface modifiers for subsequent conjugation with biomolecules [6,7]. Compared with conventional organic molecular phosphors, Ln^{3+} -doped nanocrystalline oxides have long fluorescence lifetimes (in the μs and ms range), quasilinear emission bands, broad Stokes shift, high photobleaching resistance, and comparable photoluminescence (P.L.) efficiency [8,9].

When lanthanide ions are introduced into the oxide matrix, the 4f-4f radiative electronic transitions forbidden by the Laporte Rule become partially allowed due to the admixture of opposite parity configuration 4f states. [10]. As a result, there is the possibility of the indirect P.L. excitation of the Ln^{3+} , with narrow f-f emission lines and long lifetime, through oxide nanoparticles, acting as nanoantennas [11,12]. If Ln^{3+} ions are embedded into a suitable crystal lattice, the sequential absorption of several photons through the lanthanide energy levels can occur in oxide nanoparticles, which provides higher energy to the anti-Stokes luminescence [13].

The electronic excitation energy transferred to lanthanide ions is defined by the oscillator strength, with the latter depending on the bandgap width and the refractive index of the oxide matrix [14,15]. Crystalline ZrO_2 has a large bandgap (4–6 eV), a high refractive index (2.13–2.20), and a small absorption capacity in the visible and near-infrared spectral regions in combination with low phonon energy (470 cm^{-1}), which reduces the probability of the nonradiative multiphonon relaxation of excited Ln^{3+} activator ions [16–18]. These properties, combined with the bioinertness of crystalline zirconia, make it the optimal matrix for the introduction of Ln^{3+} [19]. ZrO_2 at an ambient temperature and atmospheric pressure is present in the monoclinic phase. However, the tetragonal and cubic polymorphs can be formed by heat treatment, the inclusion of dopant metals with a lower valence into the crystal lattice, and also by increasing the surface energy of nanoparticles [20–23]. The heat treatment of zirconium dioxide at phase transition temperatures leads to an increase in crystallite size, while the phase stabilization of thermodynamically unstable tetragonal (t) and cubic (c) ZrO_2 using lanthanide ions helps to reduce the size of nanoparticles, which is preferable.

The distribution of lanthanide ions between the monoclinic and more symmetrical t and c phases of ZrO_2 can be seen in the example of europium (III) ions, used as local structural probes [24,25]. The latter fact is due to the luminescent properties of Eu^{3+} , which are very sensitive to changes in the symmetry of the crystal field [26,27]. This is manifested in the Stark splitting of the electric dipole transition ${}^5\text{D}_0\text{--}{}^7\text{F}_2$ [28,29]. With an increase in the content of europium ions in the ZrO_2 crystal structure, the phase composition of nanoparticles, the possible concentration quenching, and the P.L. efficiency depend strongly on the synthesis method and the nature of the precursors [30–38].

Z.W. Quan and others showed that for nanoparticles obtained by spray pyrolysis, the cubic polymorphic ZrO_2 modification stabilizes, regardless of the content of europium ions, and concentration quenching is observed in crystal phosphors containing more than 10 mol.% Eu^{3+} [32]. In the case of using the microwave hydrothermal synthesis method for ZrO_2 nanoparticles with a content of 0.1 mol.% (monoclinic phase), 5 mol.% (tetragonal phase) and 10 mol.% (cubic phase) Eu^{3+} , the concentration quenching of P.L. in the first two compositions was not detected [33]. The solid-phase synthesis of nanoparticles promotes the growth of emission intensity with an increase in the concentration of Eu^{3+} in the ZrO_2 matrix from 0.5 to 5 mol.%, and in the entire range of selected concentrations, the authors fixed only cubic phase zirconia [34]. $\text{ZrO}_2\text{:Eu}^{3+}$ nanophosphors were obtained by complex polymerization in [35], and the authors noted that the tetragonal phase of zirconia was formed at 4 mol.% trivalent impurity, and a cubic one at 8 mol.%. The emission intensity of Eu^{3+} reached a maximum when 4 mol.% stabilizing ions were introduced into the ZrO_2 structure. N. Tiwari and his colleagues synthesized nanophosphors with an m- ZrO_2 structure independently of the Eu^{3+} embedded amount (0.5–2.5 mol.%)

using the solution combustion technique [36], wherein a P.L. intensity maximum is observed for the sample with 2 mol.% of the lanthanide. Thus, the synthesis conditions play a vital role in the processes of the phase formation and stabilization of zirconia high-temperature modifications by introducing trivalent europium ions. For the same elemental compositions of Eu^{3+} -doped ZrO_2 nanoparticles, the use of various approaches for the synthesis leads to a different ratio of polymorphic modifications. At the same time, the structure, size and morphology of the forming ZrO_2 nanocrystallites, as well as the quantity, distribution uniformity, and localization of the Eu^{3+} active centers in their crystal lattice, determine the P.L. efficiency of the phosphors.

The work addresses the physicochemical problems of the synthesis and separation of various polymorphic modifications for nanoparticles of $\text{Zr}_{1-x}\text{Eu}_x\text{O}_{2-0.5x}$ solid solutions, which were formed under relatively soft hydrothermal conditions at a temperature of 250 °C without subsequent annealing. The use of complementary methods provides information on the predominance of one phase or another among the polymorphic modifications of the studied zirconia nanoparticles, including cubic, based on the profile of Raman spectra, X-ray diffraction patterns, and fine splitting in the P.L. spectra. Hydrothermal treatment also predetermined the presence of hydroxyl groups on the surface of the Eu^{3+} -doped ZrO_2 nanoparticles, which can then be used for conjugation with biomolecules [6]. Therefore, in connection with the biomedical aspects of the use of synthesized phosphors in composite materials, one of the study objectives was to analyze how phase stabilization with europium (III) ions affects the size, surface area and charge. Since in our work, we consider $\text{Zr}_{1-x}\text{Eu}_x\text{O}_{2-0.5x}$ nanoparticles as a possible component in the creation of a bone tissue precursor, understanding the toxicity of nanomaterials is a crucial problem [39]. To know whether nanoparticles affect fibroblasts' ability to divide, differentiate, and produce collagen and elastin precursors, we used the colorimetric assay with the tetrazolium dye 3-(4,5-dimethylthiazol-2-yl)-2,5-diphenyltetrazolium bromide (M.T.T. assay).

2. Materials and Methods

2.1. Synthesis of the $\text{Zr}_{1-x}\text{Eu}_x\text{O}_{2-0.5x}$ Nanoparticles

The reagents for the synthesis of $\text{Zr}_{1-x}\text{Eu}_x\text{O}_{2-0.5x}$ nanoparticles were used without additional purification. The content of $\text{EuO}_{1.5}$ during the synthesis of zirconia-based nanophosphors was 2, 5, 7, 10, and 15 mol.%. At the first stage, the co-precipitation of $\text{ZrO}(\text{OH})_2$ - $\text{Eu}(\text{OH})_3$ mixtures in the predetermined molar ratio from $\text{ZrOCl}_2 \times 8\text{H}_2\text{O}$ and $\text{EuCl}_3 \times 6\text{H}_2\text{O}$ solutions using ammonium hydroxide was carried out [37]. Then the zirconium and europium hydroxide compositions were dehydrated under hydrothermal conditions for 4 h at 250 °C and 15 MPa. All nanopowders after hydrothermal treatment were dried at 100 °C to a constant weight.

2.2. Characterization Methods

2.2.1. X-ray Diffraction of $\text{Zr}_{1-x}\text{Eu}_x\text{O}_{2-0.5x}$ Nanoparticles

The X-ray diffraction (X.R.D.) method was used for the structural analysis of resulting nanophosphors. The powder diffractograms were recorded using the SmartLab X-ray diffractometer (Rigaku, Japan) at $\text{CuK}\alpha$ in the 5–150° range with a scan rate of 0.5°/min. LaB_6 was used as a reference to take into account the apparatus width. The MAUD software package (L. Lutterotti, Italy) was used to determine the phase composition and calculate the parameters of a unit cell of nanoparticles [40].

2.2.2. Energy-Dispersive X-ray Microanalysis of $\text{Zr}_{1-x}\text{Eu}_x\text{O}_{2-0.5x}$ Nanoparticles

The elemental composition of synthesized nanoparticles was measured using a SUPRA 55VP (Carl Zeiss AG, Germany) scanning electron microscope (S.E.M.) with an INCA microanalysis system (Oxford Instruments, UK). Quantitative energy-dispersive X-ray (E.D.X.) microanalysis was carried out using the method of fundamental parameters. The standard accumulation time of the spectrum

was 60 s, while for the determination of the elements with small content, the time was increased to 300 s. The composition was determined from the maximum possible area of the test sample.

2.2.3. X-ray Fluorescence Analysis of $Zr_{1-x}Eu_xO_{2-0.5x}$ Nanoparticles

A qualitative/quantitative elemental analysis of nanoparticle powders was also carried out using a software-analytical complex based on the Spectroscan Max-GF2E portable X-ray fluorescence crystal diffractive spectrometer (Spectron, Russia Q5).

2.2.4. Transmission Electron Microscopy of $Zr_{1-x}Eu_xO_{2-0.5x}$ Nanoparticles with Microdiffraction

The shapes, sizes, and phase compositions of nanophosphors were investigated by the transmission electron microscope Jeol JEM-2100F (T.E.M.) at the accelerating voltage 200 kV. The sample preparation for T.E.M. included applying nanoparticle dispersions on graphene-coated copper grids [41]. Graphite lattice rings in microdiffraction images were used for the calibration of a diffraction pattern scale.

2.2.5. Raman Spectroscopy of $Zr_{1-x}Eu_xO_{2-0.5x}$ Nanoparticles

Raman measurements were carried out using LabRAM HR800 with a 1800 gr/mm diffraction grade in a backscattering geometry. Raman spectra (R.S.) were recorded using an Ar^+ laser with an excitation wavelength of 488 nm in the range of 110–700 cm^{-1} . The spectrometer was calibrated using a 520.7 cm^{-1} line of silicon standard before measurement. At the sample surface, the laser power was 13 mW under the 10x lens. Each spectrum was recorded 10 times for 10 s.

2.2.6. Surface Area and Porosity Analysis of $Zr_{1-x}Eu_xO_{2-0.5x}$ Nanoparticles

A specific surface area analysis of synthesized nanoparticles was conducted via low-temperature nitrogen adsorption with the QuantaChrome Nova 4200B analyzer (Quantachrome Instruments, Boynton Beach, FL, USA). The samples were degassed before measuring at 200 °C in vacuo for 16 h. On the basis of the data obtained, the specific surface area (S_{BET}) of nanoparticles was determined with the Brunauer–Emmett–Teller theory (B.E.T.) at seven points. The pore size distribution was assessed based on nitrogen desorption isotherms according to the Barrett–Joyner–Halenda method (B.J.H.).

2.2.7. Electrophoresis Light Scattering of $Zr_{1-x}Eu_xO_{2-0.5x}$ Nanoparticles

Electrokinetic experiments were carried out using a Malvern Zetasizer Nano Z.S. laser analyzer from Malvern Instruments (Malvern, UK) at 25 °C. Zeta (ζ) potential measurements of $Zr_{1-x}Eu_xO_{2-0.5x}$ dilute suspensions (10 mg in 100 mL) were performed at a pH value of 6.4 with a background electrolyte concentration (NaCl) of 10^{-3} M.

2.2.8. M.T.T. Assay of $Zr_{1-x}Eu_xO_{2-0.5x}$ Nanoparticles

Biological material from a skin biopsy of a young, conditionally healthy donor obtained with the observance of the septic and antiseptic rules was used to isolate dermal fibroblasts. A standard enzymatic technique was used to isolate the primary culture of dermal skin fibroblasts [42]. The cell suspension obtained during the enzymatic treatment was cultured in a complete DMEM nutrient medium (Paneco, Russia) supplemented with L-glutamine, 10% bovine fetal serum, and antibiotics in a CO_2 incubator (Thermo Fisher Scientific, 3423) at a temperature of 37 °C, a CO_2 concentration of 5%, and high humidity. Cells of 3–12 passages were used for research. The dispersion of $Zr_{1-x}Eu_xO_{2-0.5x}$ nanoparticles obtained by ultrasonic treatment was disinfected and placed in the wells of a culture plate. A cell suspension was added to the wells in a complete culture medium containing 25,000 cells, and the dermal fibroblasts were incubated for 3 days. The growth medium was replaced with 3-(4,5-dimethylthiazol-2-yl)-2,5-diphenyl-2H-tetrazolium bromide solution and incubated for 2 h. Subsequently, the solution was removed, and the formazan crystals were extracted by pouring dimethylsulfoxide into the wells. After thoroughly mixing, the resulting solution was spread over

96 wells of a culture plate. The solution absorbance was recorded using a SPECTROstar Nano spectrophotometer (B.M.G. Labtech, Germany) at a wavelength of 570 nm to determine the number of viable dermal fibroblasts in an aqueous dispersion of $Zr_{1-x}Eu_xO_{2-0.5x}$ nanoparticles. The formula for the calculation of viable cells was taken from [43].

2.2.9. Photoluminescence Quantum Yield Measurements of $Zr_{1-x}Eu_xO_{2-0.5x}$ Nanoparticles

The P.L. quantum yield of nanophosphors was measured by the modified de Mello method using a Fluorolog-3 fluorescence spectrometer equipped with a Quanta-j integrating sphere [44]. Tablets with a 10 mm diameter and thickness of 3 mm were compressed from a mixture of dry KBr, with spectroscopic-grade purity, and $Zr_{1-x}Eu_xO_{2-0.5x}$ nanoparticles in the mass ratio of 100:1. Potassium bromide without nanophosphors was used as a reference. The P.L. quantum yield measurements were carried out at an ambient temperature.

2.2.10. Photoluminescence Spectroscopy of $Zr_{1-x}Eu_xO_{2-0.5x}$ Nanoparticles

The P.L. emission spectra for $Zr_{1-x}Eu_xO_{2-0.5x}$ nanoparticle powders were studied using a luminescence spectrophotometer LS-100 (PTI[®], Canada) and a Horiba LabRAM HR Evolution system. The P.L. intensity (I_{lum}) was recorded from the side of the incidence light in the 100–2000 μ s range of an integration window for LS-100. Here, the grazing angle of the exciting light to the sample was ca. 30°. To excite photoluminescence in LS-100, we used an EG&G FX 280V 91 xenon lamp. The geometric slit width for excitation and luminescence monochromators was 1 mm, with a reciprocal linear dispersion of 4 nm/mm. A Horiba LabRAM HR Evolution system was equipped with a He–Cd excitation laser emitting at 325 nm with a maximum power of 1 mW at the sample, and it possessed a 100 grooves/mm grating and a Peltier-cooled charge-coupled device detector. The light was focused onto the sample surface thanks to a 15 \times (0.32 numerical aperture) objective. The emission spectra of the $Zr_{1-x}Eu_xO_{2-0.5x}$ nanoparticles were registered from 560 to 770 nm. The P.L. excitation spectra of the systems under investigation were recorded using LS-100 in the range of 205–400 nm. The P.L. intensities for the correct comparison led to an internal laboratory standard.

The luminescence lifetime of the $Zr_{1-x}Eu_xO_{2-0.5x}$ nanoparticles was measured in the pulsed mode of a xenon lamp based on the P.L. intensity's decay. According to the excitation spectra, we excited the P.L. at 247 and 255 nm, and its observation was carried out at 614 and 608 nm, starting from the emission spectra. The values of lifetimes (τ_{p1}) were calculated with an iterative fitting procedure using QtiPlot software [45]. Model approximation functions for the P.L. intensity decay were selected based on the χ^2 criterion.

3. Results and Discussion

3.1. Structural Study

The carried-out elemental analysis revealed that the $ZrO_2/EuO_{1.5}$ ratios specified in the synthesis pertained for the selected nanoparticle compositions. The deviation in the content of elements was about 0.5 mol.%, according to X-ray fluorescent analysis (Table 1). The S.E.M.–E.D.X. microanalysis gave a higher difference in the $EuO_{1.5}$ concentration for nanophosphors of $Zr_{1-x}Eu_xO_{2-0.5x}$, which may have been caused by the applied powders screening due to the surface relief formed as a result of sample preparation, or the dissimilarity in the approaches to processing the spectra via software.

Figure 1 illustrates the X-ray diffraction patterns for the $Zr_{1-x}Eu_xO_{2-0.5x}$ ($x = 0.02$ – 0.15) nanoparticles with different phase compositions. It shows a tetragonal/cubic crystal lattice, except for the lowest europium (III) ion content in the $Zr_{1.98}Eu_{0.02}O_{1.99}$ nanoparticles obtained from chlorides (Figure 1, pattern 1; Figure 2). The distinction between tetragonal and cubic phases when the system consists of the three polymorphic modifications is not reliable. One can talk about the predominating tetragonal phase, which is more plausible, especially if we take into account the (102) diffraction peak of t- ZrO_2 . (Along with the tetragonal phase, at high concentrations of europium (III) ions in ZrO_2 ,

the cubic one is observed using Rietveld refinement. See Table S1 in the Electronic materials' support (E.M.S.) file.)

Table 1. Size and elemental composition of $Zr_{1-x}Eu_xO_{2-0.5x}$ nanoparticles.

EuO _{1.5} Content by Synthesis Charge, mol.%	T.E.M. Nano-particle Size, ¹⁾ nm	Data of Fluorescence Analysis Calculated as Oxides, mol.%		Data of S.E.M.–E.D.X. Microanalysis Calculated as Oxides, mol.%	
		ZrO ₂	EuO _{1.5}	ZrO ₂	EuO _{1.5}
2	11.4 ± 0.2	97.8 ± 2.9	2.2 ± 0.1	97.1 ± 4.9	2.9 ± 0.2
5	13.3 ± 0.3	94.6 ± 2.8	5.4 ± 0.2	92.6 ± 4.6	7.4 ± 0.4
7	10.1 ± 0.2	92.8 ± 2.9	7.2 ± 0.2	90.5 ± 4.5	9.5 ± 0.5
10	11.1 ± 0.2	91.2 ± 2.9	8.8 ± 0.3	88.9 ± 4.4	11.1 ± 0.6
15	9.2 ± 0.2	86.4 ± 2.6	13.6 ± 0.4	88 ± 4.4	12 ± 0.6

¹⁾ Mean weighted size calculated from size distribution histograms (See E.M.S. file).

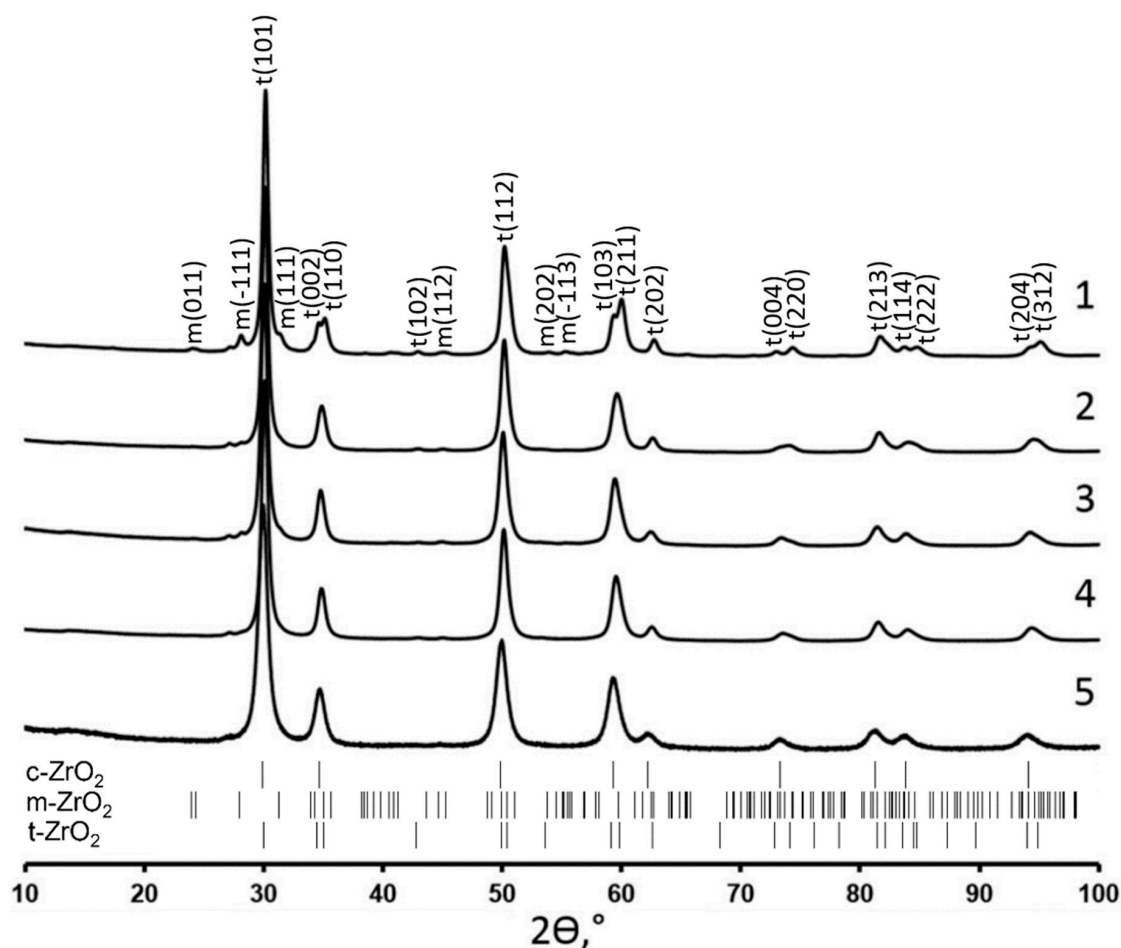


Figure 1. X.R.D. patterns of $Zr_{1-x}Eu_xO_{2-0.5x}$ nanoparticles with x equal to 0.02 (1), 0.05 (2), 0.07 (3), 0.1 (4), and 0.15 (5).

As the content of Eu^{3+} in the $Zr_{1-x}Eu_xO_{2-0.5x}$ nanoparticles increases, the (101/111) diffraction peak corresponding to the metastable zirconia phases gradually shifts from 30.17 to 29.96° , which indicates the incorporation of europium (III) ions into the t-/c- ZrO_2 crystal lattices, with the formation of solid solutions (Figure 2).

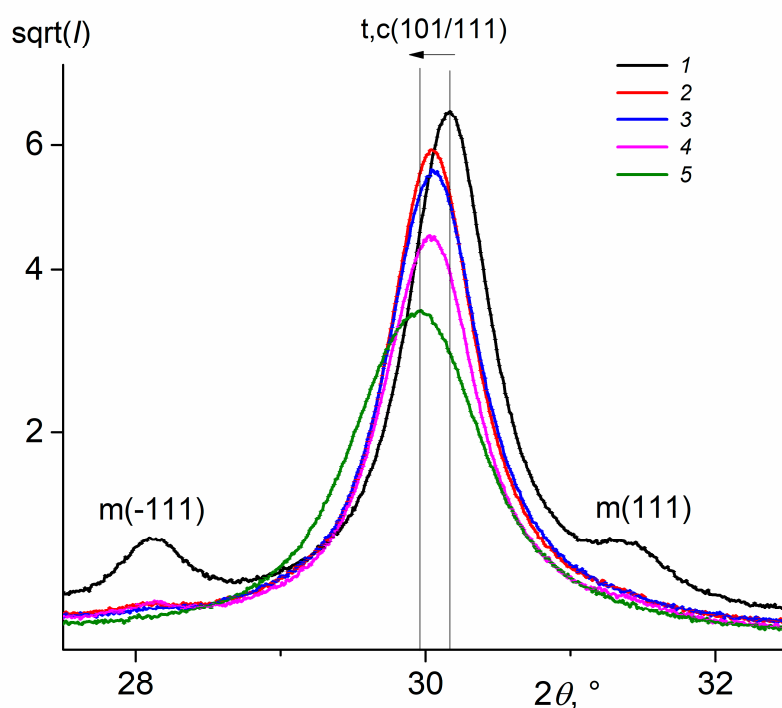


Figure 2. The 2θ range of 28–32° in X.R.D. patterns upon varying the Eu^{3+} content in $\text{Zr}_{1-x}\text{Eu}_x\text{O}_{2-0.5x}$ nanoparticles at x equal to 0.02 (1), 0.05 (2), 0.07 (3), 0.10 (4), and 0.15 (5).

The synthesized nanoparticles have a predominantly spherical-like shape (Figure 3a, rows 1 and 2), but as the content of europium (III) ions increases in the ZrO_2 matrix, the proportion of crystallites with cubic faceting grows (Figure 3a, rows 3–5), according to the T.E.M. data. Table S3 shows descriptive statistics (mode, median, mean, mean weighted and index of dispersity) based on microphotographs of the T.E.M. and the analysis of size distribution histograms (Figure 3c).

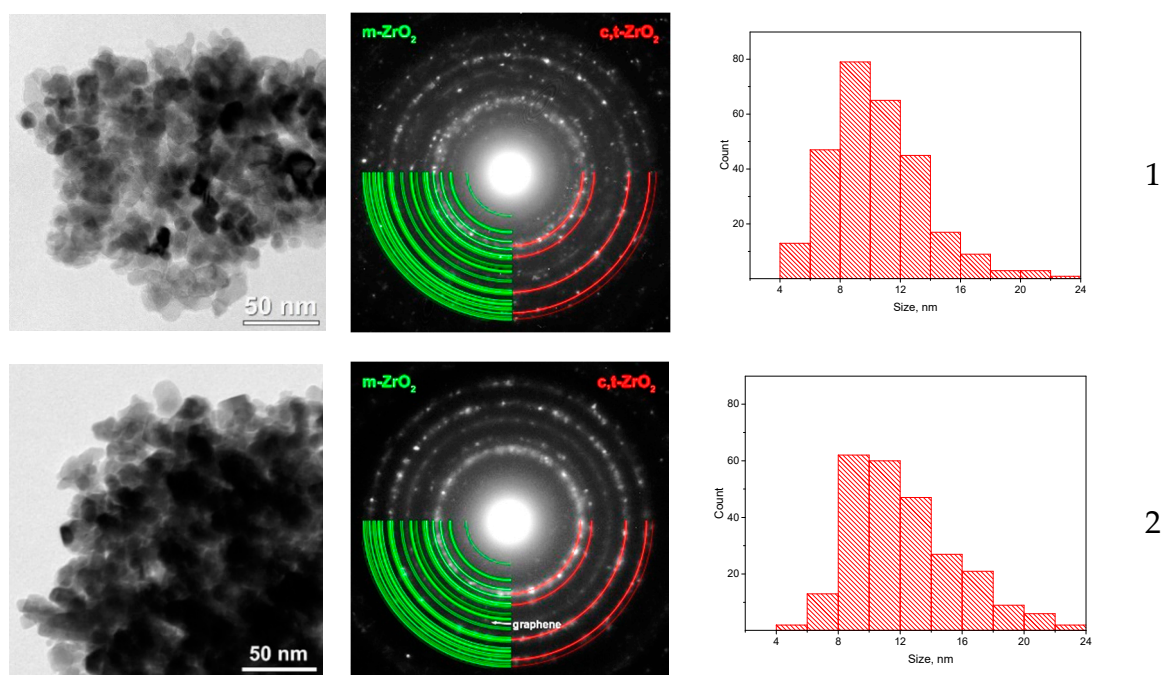


Figure 3. Cont.

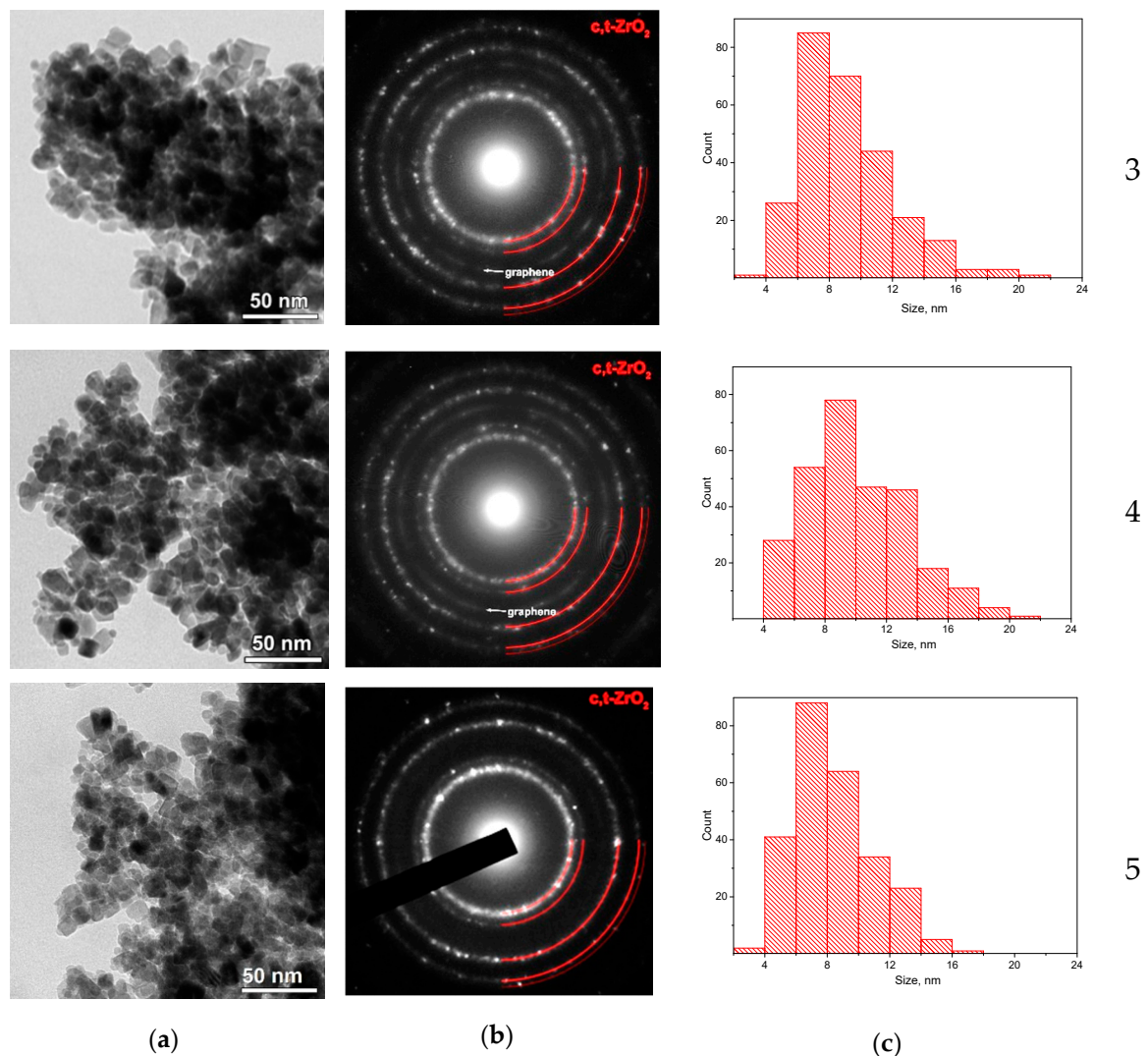


Figure 3. TEM micrographs (a), electronic diffraction patterns (b) and size distribution histograms (c) of $Zr_{1-x}Eu_xO_{2-0.5x}$ nanoparticles with x equal to 0.02 (1), 0.05 (2), 0.07 (3), 0.1 (4), and 0.15 (5).

Phase composition changes of nanoparticles, following the increase in the Eu^{3+} content in the ZrO_2 structure, were also analyzed using normalized R.S. (Figure 4). Nanoparticles with 2 mol.% $EuO_{1.5}$ are characterized by Raman shifts at 178, 335, 474, 533, 556, 613, and 636 cm^{-1} , corresponding to the m - ZrO_2 phase. Strong peaks appear at 178, 335, and 474 cm^{-1} (Figure 4, curve 1). The set of peaks at 149, 224, 266, 324, 407, 459 and 639 cm^{-1} makes it easy to identify the tetragonal phase of ZrO_2 , which is present in all the nanoparticle compositions under study [46]. The Raman spectra of the high-temperature metastable cubic phase of ZrO_2 have a narrow peak at 149 cm^{-1} , and wide, poorly resolved ones in the ranges 230–290 cm^{-1} , 400–430 cm^{-1} and 530–670 cm^{-1} , which appear when the $EuO_{1.5}$ content is 10 or 15 mol.% (Figure 4, curves 3–5) [47]. The observed Raman peak of 149 cm^{-1} is common to both the tetragonal and cubic phases [48]. It should be noted that the cubic ZrO_2 demonstrates an amorphous spectrum of Raman scattering with one wide band at 530–670 cm^{-1} [49]. We observed the above band with a maximum at 611 cm^{-1} in the Raman spectrum for ZrO_2 nanoparticles containing 15 mol.% $EuO_{1.5}$ (Figure 4, curve 5), whereas the predominantly tetragonal ZrO_2 shows clearly visible bands at 460 and 640 cm^{-1} due to its lower symmetry [50] (Figure 4, curves 1–3).

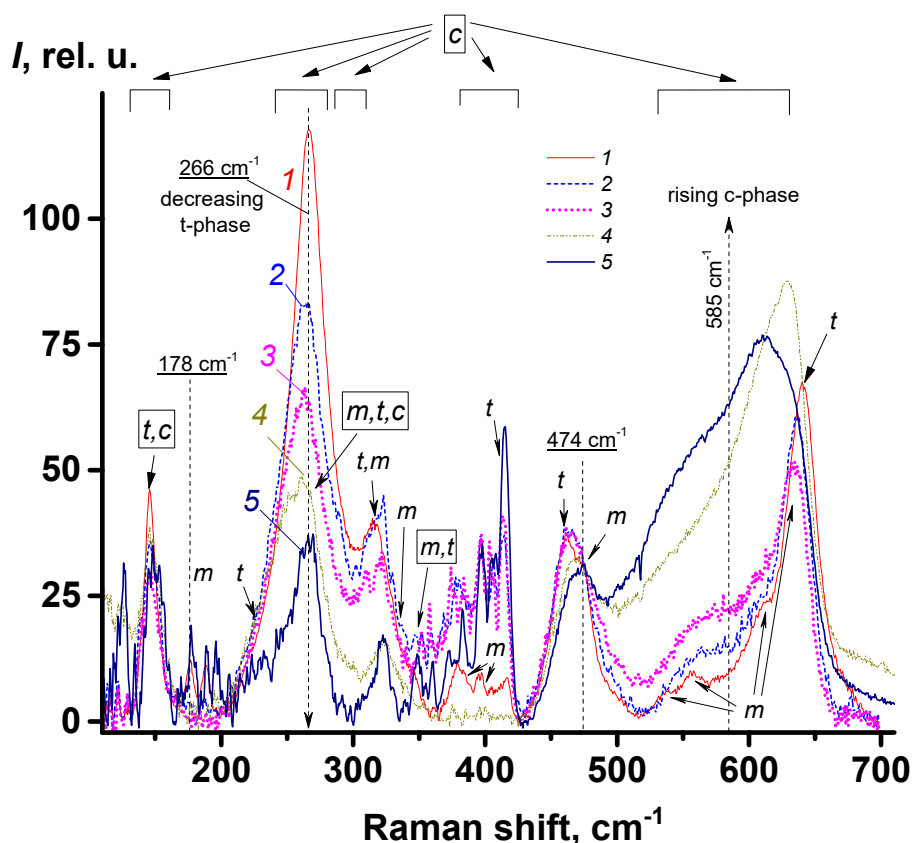


Figure 4. Raman spectra of $Zr_{1-x}Eu_xO_{2-0.5x}$ nanoparticles with x equal to 0.02 (1), 0.05 (2), 0.07 (3), 0.1 (4), 0.15 (5) and the m-, t- and c-phase content varying in these nanoparticles. Raman spectra are normalized at 474 cm^{-1} .

Along with the X.R.D. data obtained by the Rietveld refinement (Figure 2), the Raman spectra indicate the c-phase increases as the content of Eu^{3+} grows, which is seen in Figure 4 at 585 cm^{-1} . Unfortunately, the cubic (single) F_{2g} mode around 630 cm^{-1} is rather weak and hidden in the much stronger phonon bands of the tetragonal phase. Here, the tetragonal ZrO_2 behaves anti-symbatically with the cubic phase as the Eu^{3+} content increases. In R.S., this corresponds to a decrease in t- ZrO_2 contribution at 266 cm^{-1} (Figure 4).

Besides this, the scattering band in the range $530\text{--}670\text{ cm}^{-1}$ shifts to the smaller wave numbers, from the peak at 640 cm^{-1} for zirconia nanoparticles containing 2 mol% $EuO_{1.5}$ (Figure 4, curve 1) to the peak with a maximum at 611 cm^{-1} for the $Zr_{0.85}Eu_{0.15}O_{1.925}$ composition (Figure 4, curve 5). This result is also confirmed by a decrease in the intensity of scattering at 460 cm^{-1} with a Eu^{3+} content increase in the ZrO_2 crystal lattice (Figure 4).

3.2. Photoluminescence Properties

The P.L. spectra for $Zr_{1-x}Eu_xO_{2-0.5x}$ ($x = 0.02 \div 0.15$) nanoparticles are presented in Figure 5. The peaks observed at 591, 606, 614, 624, 633, 651, 657, 701 and 748 nm, as well as the shoulder at 580 nm, can be compared with the spectral terms of the Stark splitting $^5D_0 \rightarrow ^7F_J$ ($J=0\text{--}6$) for the radiative transitions in the Dieke diagram of the $Eu^{3+} 4f^6$ configuration [14,51,52].

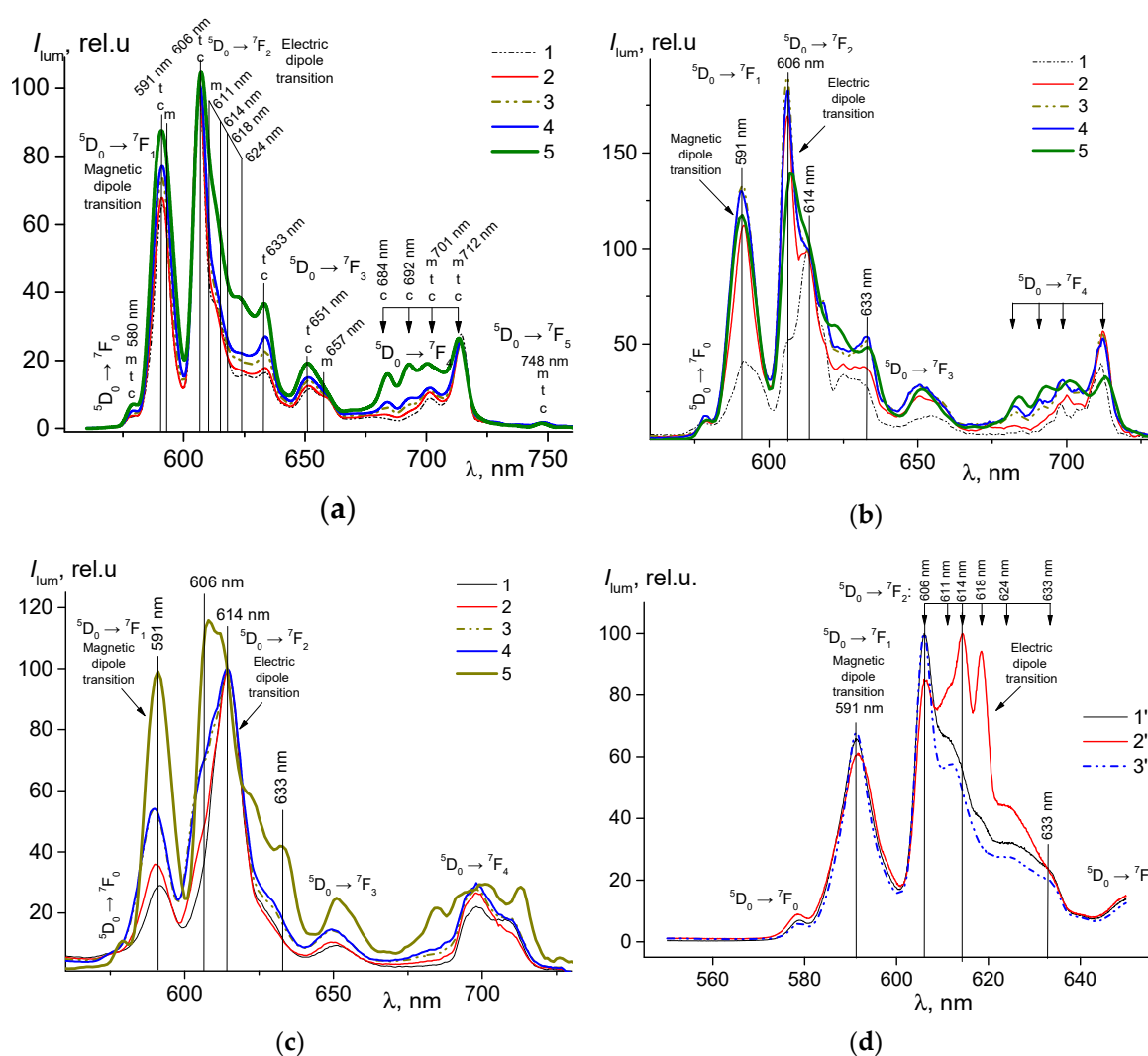


Figure 5. Normalized at 606 and 614 nm, luminescence spectra of $Zr_{1-x}Eu_xO_{2-0.5x}$ nanoparticles with x equal to 0.02 (1), 0.05 (2), 0.07 (3), 0.1 (4) and 0.15 (5). The P.L. excitation was at 255 (a), 270 (b) and 397 nm (c); in the case of the $Zr_{0.85}Eu_{0.15}O_{1.925}$ composition (d), at 267 (1'), 300 (2') and 397 nm (3').

The excitation spectra (Figure 6) for the $Zr_{1-x}Eu_xO_{2-0.5x}$ nanoparticles cover the range of intraconfiguration $4f^N \rightarrow 4f^N$ transitions in the region of 270–490 nm. Besides this, the excitation band with the maximum peak at 240 nm and several additional local extremums at 227, 256 and 265 nm corresponds to the $O^{2-}-Eu^{3+}$ charge transfer originating from electronic transitions from the 2p orbital of O^{2-} to the 4f orbital of the Eu^{3+} [30,53,54]. In our case, the excitation wavelengths (λ_{exc}) of 255, 270 and 397 nm were chosen based on the excitation spectra needed to obtain P.L. It is known that the contributions of intensity in the P.L. spectrum at 606 and 633 nm are associated with the tetragonal and cubic phases of zirconia, the maximum at 614 with the shoulder at 624 nm being assigned to the ZrO_2 monoclinic allomorph [29,55]. The fact that the crystalline field of different allomorphs may split the luminescence band Eu^{3+} in different ways was previously shown in [28]. The presence of Eu^{3+} multisites across a single phase and the co-presence of multiple allomorphs complicates any reliable analysis of its Stark structure. Besides, it should be remarked that the ${}^5D_0 \rightarrow {}^7F_2$ peak does not split in the statistically non-symmetric environment formed by the Eu^{3+} -polymeric complexes, either in bulk or solution [52].

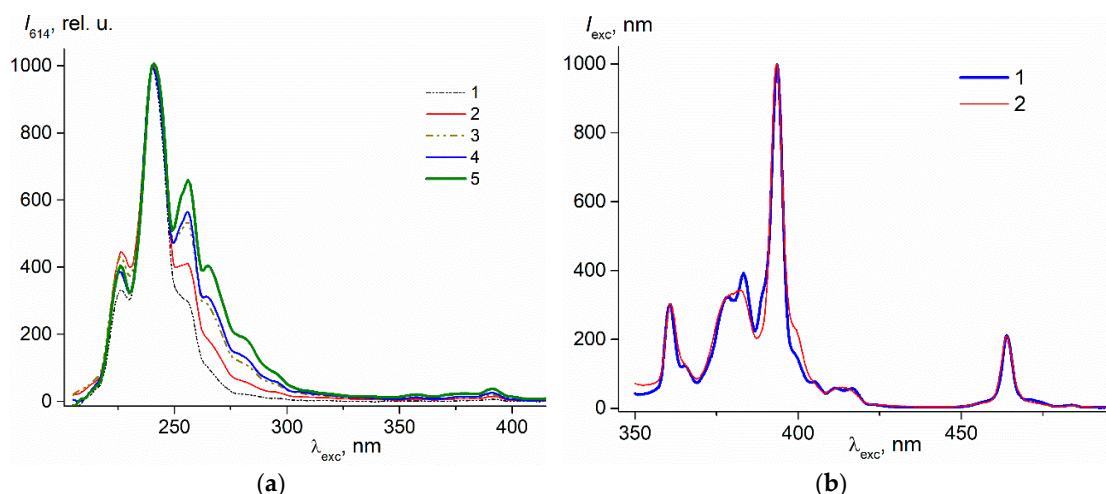


Figure 6. Normalized at 240 nm, excitation spectra (a) of $Zr_{1-x}Eu_xO_{2-0.5x}$ nanoparticles with x equal to 0.02 (1), 0.05 (2), 0.07 (3), 0.1 (4) and 0.15 (5). P.L. was observed at 606 nm. The P.L. excitation spectra (b) normalized at 393 nm for $Zr_{0.95}Eu_{0.05}O_{1.975}$ nanoparticles were observed at 606 (1) and 614 nm (2).

The appearance of the high symmetry phases (tetragonal/cubic) of ZrO_2 is evident in the P.L. spectra when the content of $EuO_{1.5}$ in nanoparticles is 5 mol.% or more (Figure 5, curves 2–5). Its fraction is shown to rise upon increasing the Eu^{3+} content, according to the P.L. spectra at all used values of λ_{exc} . In this case, the I_{lum} contribution grows at 606 nm and 633 nm in the P.L. spectra (Figure 5a–c). The spectral term 7F_4 splitting into several components with clear peaks at 684, 692, 701, and 712 nm (Figure 5a,b) proves the high symmetry of the t-/c- ZrO_2 phase. However, we should note the splitting of nine lines for monoclinic symmetry, seven for tetragonal, and four for cubic indicates the single center distribution and the multisite one, which is the case for Eu^{3+} in ZrO_2 [26,27]. As a result, it is difficult to conclude on this or that symmetry for the zirconia crystal lattice. However, what needs to be noted is that the index characterizing the environmental symmetry of Eu^{3+} in the zirconia crystal lattice was estimated as the ratio of intensities of the magnetic (I_{591}) and electric ($I_{max\ 606, 614}$) dipole transitions from the P.L. spectra (Figure 5a–c) [25]. This systematically increases from 0.65 to 0.87 at $\lambda_{exc} = 255$ nm, from 0.41 to 0.71 at $\lambda_{exc} = 270$ nm, and from 0.29 to 0.54 at $\lambda_{exc} = 397$ nm for the t-/c- ZrO_2 phase.

The presence of monoclinic zirconia along with high symmetry phases of $Zr_{1-x}Eu_xO_{2-0.5x}$ nanoparticles at $x = 0.05$ – 0.15 is confirmed in the P.L. spectra by a significant contribution at 614 and 624 nm (Figure 5b–c) [29,55]. The existence of m- ZrO_2 was also inferred from the peaks in the Raman spectra at 178, 336 and 474 cm^{-1} (Figure 4). The X.R.D. method has shown that its quantity at $x \geq 0.05$ can be expected to be no more than 2%. Tiseanu C. et al. in their article discuss ordered and disordered monoclinic phases [28]. We found that in the luminescence spectra, the m- ZrO_2 phase manifests itself against a tetragonal/cubic contribution, which is associated with the possible uneven segregation of europium (III) ions. According to the phase diagram given in [56], we can talk about the uneven isolation (segregation) of europium (III) ions along the grain of the different phases. In the P.L. spectra at excitations of 270, 300 and 325 nm, the segregation of Eu^{3+} between phases is made particularly evident for $Zr_{0.85}Eu_{0.15}O_{1.925}$ by comparing the peaks at 614 nm with 606 and 633 nm (cf. curves 4 and 5 in Figure 5b, as well as Figure 5d, curve 2'; cf. curve 4 with 2 and 3 in Figure S2).

Moreover, the profile of the P.L. spectra depends on the excitation wavelengths. The higher symmetry phases, such as t- and c- ZrO_2 , show themselves at 606 and 633 nm (Figure 5a,b) in the range of interconfiguration and charge-transfer state transitions upon excitation at 255 and 270 nm (Figure 6a). The significant contribution of the less symmetric m- ZrO_2 phase appears at 397 nm as a result of the intrinsic absorption of Eu^{3+} (Figure 5c). Changing the excitation wavelength proves this effect for $Zr_{0.85}Eu_{0.15}O_{1.925}$ nanoparticles clearly (Figure 5d). It turned out that in the P.L. band, we could observe six components (606, 611, 614, 618, 624, and 633 nm) in the splitting of ${}^5D_0 \rightarrow {}^7F_2$ for nanoparticles with

15 mol.% $\text{EuO}_{1.5}$ at $\lambda_{\text{exc}} = 300$ nm. This result is accounted for by the europium (III) ions found in more than one local environment. They work as luminescent probes for investigating the complex media environment [57]. In the term ${}^7\text{F}_2$ of the P.L. band, the two lines of Stark splitting are responsible for the cubic symmetry, and the four ones are because of the occurrence of the t-phase environment [27]. This Stark splitting evidences the two regular ionic arrangements in the nanoparticles' crystal lattice, at least. Stated differently, varying the excitation wavelength is sufficient to enable the m- ZrO_2 to be recognized against the prevalent metastable phases.

It should be noted that when the intraconfigurational transitions are excited in the region of 270–397 nm, the contribution of P.L. intensity at 614 nm grows in the excitation spectra (Figure 6a) upon increasing the Eu^{3+} content. Moreover, in the excitation region of 395–405 nm for ZrO_2 nanoparticles with 5 mol.% $\text{EuO}_{1.5}$, one can infer the increase in the contribution of the m-phase from the P.L. intensities observed at 614 nm, as compared with the t-/c- ZrO_2 which appeared at 606 nm (cf. curve 1 and 2, Figure 6b).

Figure 7 shows the P.L. intensity decays $I_{\text{lum}}(t)$ of Eu^{3+} in the ZrO_2 matrix. The systems under study are sensitive to the wavelength of excitation; in addition, they consist of particles in metastable states with microstrains and excess energy at the border. In this regard, it is possible to expect the wide spectrum of times characterizing the luminescence lifetime for Eu^{3+} as a probe. Therefore, in this work, we used the “stretched” exponential function to describe luminescence decay. The parameters for the obtained P.L. lifetimes are given in Table 2. The stretched exponential function is used following A. Werner (1907) and T. Förster (1949) to approximate the P.L. decay for phosphors dwelling in multiple-type environments [58]:

$$I_{\text{lum}}(t) = I_0 e^{-\left(\frac{t-t_0}{\tau_{\text{P.L.}}}\right)^\beta} - B \quad (1)$$

where t is decay time, I_0 is the luminescence intensity at $t = 0$, $\tau_{\text{P.L.}}$ is the photoluminescence lifetime, t_0 is the time shift in the observation channels, and B is background of a signal under a “dark” condition. The value of β is the stretched exponential parameter ($0 \leq \beta \leq 1$), with which the width of the luminescence lifetime spectrum in the excited states can be characterized as $D_f = 2 - \beta$.

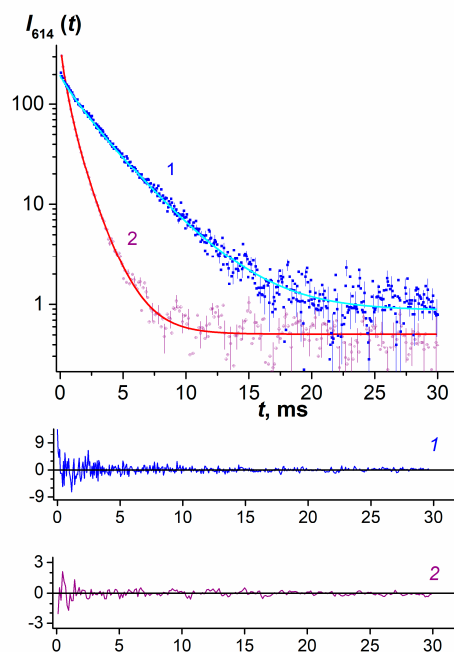


Figure 7. Photoluminescence decay for $\text{Zr}_{1-x}\text{Eu}_x\text{O}_{2-0.5x}$ nanoparticles with x equal to 0.02 (1), 0.15 (2). P.L. was observed at 606 nm and excited at 247 (1) and 255 nm (2).

Table 2. Comparison of P.L. lifetime, τ_{PL} , and quantum yield, φ , for $Zr_{1-x}Eu_xO_{2-0.5x}$ nanoparticles upon excitation at 262 nm and observation at 614 nm.

EuO _{1.5} Content by Synthesis, mol.%	φ , %	τ_{PL} ,ms	β	$D_f = 2 - \beta$	$\chi_{red}^{2\ 1)}$
2	0.54	0.84 ± 0.43	0.70 ± 0.12	1.30	12.54
5	0.63	0.27 ± 0.02	0.638 ± 0.019	1.362	8.37
7	1.16	0.33 ± 0.01	0.633 ± 0.012	1.367	4.93
10	1.25	0.83 ± 0.28	0.81 ± 0.10	1.19	12.49
15	2.11	0.28 ± 0.04	0.62 ± 0.02	1.39	1.76

¹ The reduced Chi-square parameter, χ_{red}^2 , which equals the residual sum of squares divided by the degree of freedom and is used in Pearson's chi-square test of fit goodness to establish whether an observed experimental curve differs from a theoretical one.

It was found that the values of τ_{PL} occur in the range of 0.27–0.84 ms. This fact can be connected with the low P.L. quantum yield (φ). The widths of the lifetime spectra were almost equal, according to the value of D_f (Table 2).

It turned out that the quantum yield of $Zr_{1-x}Eu_xO_{2-0.5x}$ nanoparticles ($x = 0.02$ – 0.15), obtained from zirconyl and europium chlorides by ammonia co-precipitation and hydrothermal treatment, is no more than 3%.

3.3. Surface Properties

The values of specific surface area (S_{BET}) for the nanocrystalline samples of the ZrO_{2-x} mol.% $EuO_{1.5}$ composition with $x = 2, 5, 7, 10$ and 15 , obtained by hydrothermal synthesis, are presented in Table 3. The data indicate a slight growth of the S_{BET} value from 80.2 to 87.4 m^2/g with an increase in the $EuO_{1.5}$ concentration in the ZrO_2 crystal lattice from 2 to 10 mol.%. The introduction of 15 mol.% $EuO_{1.5}$ leads to a drastical increase (ca. 20%) in the S_{BET} to 111.3 m^2/g . At the same time, the form of sorption isotherms for these powders is practically independent of the stabilizing ion concentration. All isotherms belong to the IV type with a strongly pronounced loop of capillary-condensation hysteresis of H2 type, characteristic for mesoporous materials with bottle-shaped pores (Figure 8).

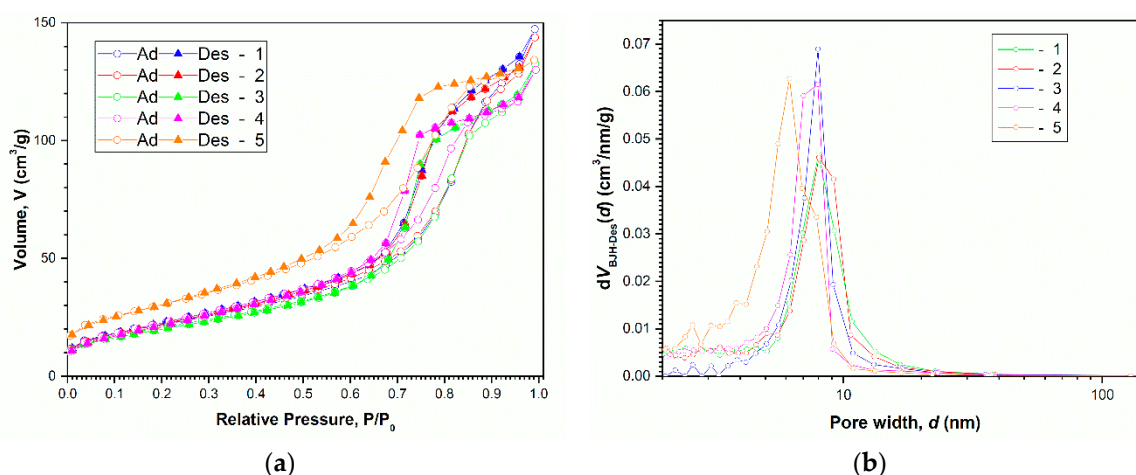
**Figure 8.** Adsorption–desorption isotherms (a) and B.J.H. distributions of pore size (b) for $Zr_{1-x}Eu_xO_{2-0.5x}$ nanoparticles with x equal to 0.02 (1), 0.05 (2), 0.07 (3), 0.1 (4) and 0.15 (5).

Table 3. The surface properties of $Zr_{1-x}Eu_xO_{2-0.5x}$ nanopowders, determined by the method of low-temperature nitrogen adsorption and electrophoretic light scattering.

EuO _{1.5} Content by Synthesis, mol. %	S _{BET} , m ² /g	D _{pore} , nm	V _{pore} , ¹ cm ³ /g	ζ-potential, mV
2	80.2 ± 2.4	8.01	0.24	−8.7
5	82.2 ± 3.3	8.04	0.23	3.1
7	85.5 ± 1.9	7.97	0.21	11.1
10	87.4 ± 3.9	7.96	0.21	14.9
15	111.3 ± 3.4	6.19	0.22	16.3

¹ The specific volume of pores is determined by the limiting filling ($P/P_0 = 0.99$).

The pore size distribution of ZrO_2 nanopowders with different Eu^{3+} contents calculated for the desorption branch according to the B.J.H. algorithm is shown in Figure 8b. The lognormal distribution of mesopores in the range of 4 to 20 nm, with a maximum of 8 nm, is observed for all samples, except nanoparticles with a concentration of europium (III) ions equal to 15mol.%. For the latter, the pore size maximum is fixed as 6 nm.

On the surface of undoped ZrO_2 nanoparticles, there are terminal hydroxyl groups associated with zirconium (IV) ions, as well as the tribridged Zr_3OH moieties (Figure 9) [59,60]. The mono-coordinated $ZrOH$ bonds exhibit acidic properties, which lead to the negative charge of the nanoparticle's surface, i.e., to the formation of the ZrO^- inner coating of the electrical double layer with negative φ -potential [61]. In the outer coating, the positive counterion-presented protons (hydroxonium ions) are adsorbed. Thus, a negative ζ -potential exists at the surface of the hydrodynamic shear, which separates the Stern layer of the positive ions strongly attached to the negatively charged nanoparticle from the counterions' diffuse layer. In the case of the isomorphic substitution of Zr^{4+} ions by Eu^{3+} , during the synthesis, the stabilization of the ZrO_2 high-temperature phases occurs. The formation of t-/c- ZrO_2 is accompanied by a decrease in the size of nanoparticles, and an increase in their surface energy, as well as their S_{BET} values. Moreover, the isomorphic incorporation of Eu^{3+} into the ZrO_2 matrix reduces the surface concentration of both negatively charged sites and terminal hydroxyls, which is manifested in a charge sign alteration for the electrokinetic potential (Figure 9) [62]. This effect is caused by lower europium (III) electrovalence compared to zirconium (IV). Besides this, the Eu^{3+} ions can also coordinate protons [61]. At a high local concentration on the surface, they can exhibit the properties of Lewis acid as well, attaching a water molecule [63]. This circumstance leads to the appearance of an excess of positive charge on the surface and the emergence of a positive ζ -potential (Table 3). Therefore, a further increase in the europium (III) content in the zirconia matrix contributes to a monotonous growth in the electrokinetic potential from 3.1 to 16.3 mV, with a fixed background electrolyte concentration ($10^{-3}M$ NaCl) and a pH of 6.4 for the nanoparticle dispersion.

3.4. Biological Properties

The changes in the phase composition, size, specific surface area and electrokinetic potential are reflected in the biological activity of the nanoparticles under study. The proliferation activity of human fibroblasts is preserved after three cultivation days of cells in the aqueous dispersion of $Zr_{1-x}Eu_xO_{2-0.5x}$ nanoparticles following the M.T.T. assay. This fact indicates the absence of cytotoxic properties in nanoparticles (Figure 10). However, compared to the control sample, the proliferation activity of cells in aqueous dispersions of $Zr_{1-x}Eu_xO_{2-0.5x}$ nanoparticles is lower. An increase in the nanoparticle concentration from 5 to 500 $\mu g/mL$ leads to a reduction in the survival of fibroblast cells by approximately one and half times (Figure 10, column 1).

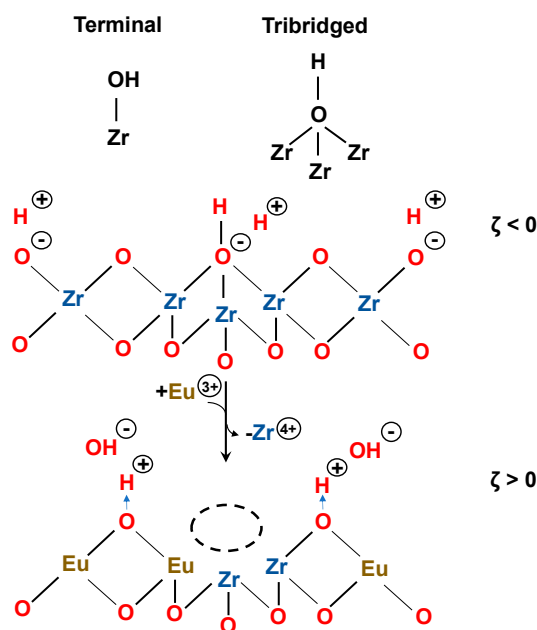


Figure 9. Scheme of chemical change on the surface of $Zr_{1-x}Eu_xO_{2-0.5x}$ nanoparticles upon doping them with Eu^{3+} .

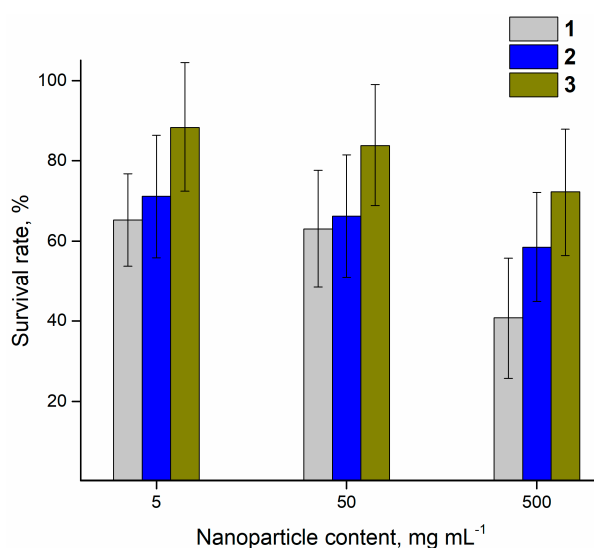


Figure 10. M.T.T. assay on human dermal fibroblasts in the dispersions of $Zr_{1-x}Eu_xO_{2-0.5x}$ nanoparticles with x equal to 0.02 (1), 0.1 (2) and 0.15 (3).

A much higher survival rate is recorded for suspensions of zirconia nanopowders with a high content of europium ions, which is due to both the ζ -potential increasing and the nanoparticle size decreasing in the range of $EuO_{1.5}$ content from 2 to 15 mol.% (Figure 10, Column 3). The above two parameters can impact the absorption of nanoparticles by transfer through the cell membrane using the mechanism of pinocytosis, as one of the two types of endocytosis, which is the absorption of liquid and dissolved substances with small bubbles up to 150 nm in diameter. Thus, all five types of $Zr_{1-x}Eu_xO_{2-0.5x}$ nanoparticles under investigation can penetrate fibroblasts due to pinocytosis. The data obtained are consistent with those previously published by Patil et al. [64], as well as Chen et al. [61]. Patil et al. suggested that negatively charged nanoparticles may interact with the positive sites on the surface of the mainly negatively charged cellular membrane [64]. In the locus of interaction, the absorbed substance is gradually surrounded by a small area of plasma membrane, which is first

invaginated and is then split off to form an intracellular bubble containing the nanoparticles captured by the cell.

4. Conclusions

For the $Zr_{1-x}Eu_xO_{2-0.5x}$ ($x = 0.02 \div 0.15$) phosphors synthesized under hydrothermal conditions over 4 h at 250 °C and 15 MPa, we managed to analyze systematically the polymorphic modifications present in the nanoparticles by X.R.D., microdiffraction of T.E.M. and R.S., together with the luminescence data.

The question of the reliable recognition of the cubic phase against the tetragonal background, despite the use of several complementary methods for the study of $Zr_{1-x}Eu_xO_{2-0.5x}$ nanoparticles, remains open. It can be said with a high degree of confidence that mainly nanoparticles are obtained from the tetragonal polymorphic modification in the range of $x = 0.02 \div 0.10$. However, it should be noted that the Rietveld refinement allowed us to assume the predominance of the cubic polymorphic modification in the $Zr_{0.85}Eu_{0.15}O_{1.925}$ nanoparticles (see the E.M.S. file).

Moreover, an increase in the $EuO_{1.5}$ mole fraction of $Zr_{1-x}Eu_xO_{2-0.5x}$ nanophosphors formed under conditions of hydrothermal synthesis contributes to the pronounced splitting of the ${}^5D_0 \rightarrow {}^7F_J$ ($J = 2$ and 4) spectral terms. To gain a quantum yield more than 3%, one needs to use more perspective organic lanthanide (III) precursors in the hydrothermal synthesis of $Zr_{1-x}Eu_xO_{2-0.5x}$ nanoparticles.

The use of different amounts of europium (III) ions in the hydrothermal synthesis of ZrO_2 -based phosphors allows for varying the ζ -potential and the size of nanoparticles, which is required to create either biocompatible or cytotoxic nanoparticles. In the future, such nanoparticles can potentially be used both as biomarkers and in the functionalization of organic–inorganic composites for biomedical applications. However, this requires additional research.

Supplementary Materials: The following are available online at <http://www.mdpi.com/2073-4352/10/11/1038/s1>, the text file in PDF format.

Author Contributions: A.N.B. and R.Y.S. thought out and formed the general concept of the research, made and analyzed X.R.D. experiments, studied photoluminescence properties of the nanoparticles and wrote the article; A.N.B. and A.Y.Z. synthesized $Zr_{1-x}Eu_xO_{2-0.5x}$ nanoparticles with different contents of europium (III) ions under hydrothermal conditions; A.Y.Z. measured the elemental composition of nanophosphors; G.P.K. and T.V.K. performed studies of nanoparticle powders using the method of low-temperature nitrogen adsorption and analyzed their surface properties; D.A.K. characterized particles using T.E.M.; I.E.K. carried out measurements and calculations of quantum yields for the nanoparticles synthesized in the article; D.V.P. determined the phase composition of nanocrystallites depending on the Eu^{3+} content using Raman spectroscopy; V.A.B., C.L. investigated the samples by the electrophoresis light scattering method. All authors have read and agreed to the published version of the manuscript.

Funding: This research received no external funding.

Acknowledgments: X-ray diffraction experiments were performed on the Engineering Center equipment of the St. Petersburg State Technological Institute (Technical University). T.E.M. studies were carried out in the Federal Joint Research Center “Material science and characterization in advanced technology”. The quantum yield and Raman spectroscopy measurements were made at the Center for Optical and Laser Materials Research, St. Petersburg State University. The authors express appreciation to Kryukov A.E. representing the Institute of Macromolecular Compounds R.A.S. for the cytotoxicity studies. Ruslan Yu. Smyslov is thankful for the EU-H2020 research and innovation programme under agreement No 654360 having benefitted from the access provided by CEA/LETI in Grenoble within the framework of the NFFA-Europe Transnational Access Activity.

Conflicts of Interest: The authors declare no conflict of interest.

References

1. Xu, W.; Chang, Y.; Lee, G.H. Biomedical applications of lanthanide oxide nanoparticles. *J. Biomater. Tissue Eng.* **2017**, *7*, 757–769. [[CrossRef](#)]
2. Gai, S.; Li, C.; Yang, P.; Lin, J. Recent progress in rare earth micro/nanocrystals: Soft chemical synthesis, luminescent properties, and biomedical applications. *Chem. Rev.* **2014**, *114*, 2343–2389. [[CrossRef](#)] [[PubMed](#)]
3. Dacosta, M.V.; Doughan, S.; Han, Y.; Krull, U.J. Lanthanide upconversion nanoparticles and applications in bioassays and bioimaging: A review. *Anal. Chim. Acta* **2014**, *832*, 1–33. [[CrossRef](#)] [[PubMed](#)]

4. Tu, D.; Zheng, W.; Liu, Y.; Zhu, H.; Chen, X. Luminescent biodetection based on lanthanide-doped inorganic nanoprobos. *Co-ord. Chem. Rev.* **2014**, *29*, 13–29. [[CrossRef](#)]
5. Chen, X.; Liu, Y.; Tu, D. *Lanthanide-Doped Luminescent Nanomaterials: From Fundamentals to Bioapplications*; Springer Science & Business Media: Berlin/Heidelberg, Germany, 2013; p. 208. [[CrossRef](#)]
6. Ceja-Fdez, A.; López-Luke, T.; Oliva, J.; Vivero-Escoto, J.; Gonzalez-Yebra, A.L.; Rojas, R.A.R.; Martínez-Pérez, A.; De La Rosa, E. Labeling of HeLa cells using $\text{ZrO}_2\text{:Yb}^{3+}\text{-Er}^{3+}$ nanoparticles with upconversion emission. *J. Biomed. Opt.* **2015**, *20*, 046006. [[CrossRef](#)]
7. Liu, Y.; Tu, D.; Zhu, H.; Ma, E.; Chen, X. Lanthanide-doped luminescent nano-bioprobes: From fundamentals to biodetection. *Nanoscale* **2013**, *5*, 1369–1384. [[CrossRef](#)]
8. Liu, Y.; Zhou, S.; Tu, D.; Chen, Z.; Huang, M.; Zhu, H.; Ma, E.; Chen, X. Amine-functionalized lanthanide-doped zirconia nanoparticles: Optical spectroscopy, time-resolved fluorescence resonance energy transfer biodetection, and targeted imaging. *J. Am. Chem. Soc.* **2012**, *134*, 15083–15090. [[CrossRef](#)]
9. Luo, W.; Liu, Y.; Chen, X. Lanthanide-doped semiconductor nanocrystals: Electronic structures and optical properties. *Sci. China Mater.* **2015**, *58*, 819–850. [[CrossRef](#)]
10. Maciel, G.S.; Rakov, N.; Rakov, N. Photon conversion in lanthanide-doped powder phosphors: Concepts and applications. *RSC Adv.* **2015**, *5*, 17283–17295. [[CrossRef](#)]
11. Chakraborty, A.; Debnath, G.H.; Saha, N.R.; Chattopadhyay, D.; Waldeck, D.H.; Mukherjee, P. Identifying the correct host–guest combination to sensitize trivalent lanthanide (guest) luminescence: Titanium dioxide nanoparticles as a model host system. *J. Phys. Chem. C* **2016**, *120*, 23870–23882. [[CrossRef](#)]
12. Soares, M.R.; Rodrigues, J.; Santos, N.F.; Nico, C.; Carvalho, R.G.; Fernandes, A.J.S.; Graça, M.P.; Rino, L.; Neves, A.J.; Costa, F.M.; et al. Prospects on laser processed wide band gap oxides optical materials. In *Proceedings of the Oxide-Based Materials and Devices IV*; SPIE: Bellingham, WA, USA, 2013; Volume 8626, p. 862607.
13. Sarkar, D.; Ganguli, S.; Samanta, T.; Mahalingam, V. Design of lanthanide-doped colloidal nanocrystals: Applications as phosphors, sensors, and photocatalysts. *Langmuir* **2019**, *35*, 6211–6230. [[CrossRef](#)] [[PubMed](#)]
14. Tamrakar, R.K.; Bisen, D.; Upadhyay, K.; Tiwari, S. Synthesis and thermoluminescence behavior of $\text{ZrO}_2\text{:Eu}^{3+}$ with variable concentration of Eu^{3+} doped phosphor. *J. Radiat. Res. Appl. Sci.* **2014**, *7*, 486–490. [[CrossRef](#)]
15. Morales-Ramírez, A.D.J.; García-Murillo, A.; Carrillo-Romo, F.; García-Hernández, M.; Palmerin, J.M.; Guerrero, R.R. Preparation and scintillating properties of sol-gel Eu^{3+} , Tb^{3+} co-doped Lu_2O_3 nanopowders. *Int. J. Mol. Sci.* **2011**, *12*, 6240–6254. [[CrossRef](#)]
16. Gallino, F.; Di Valentin, C.; Pacchioni, G. Band gap engineering of bulk ZrO_2 by Ti doping. *Phys. Chem. Chem. Phys.* **2011**, *13*, 17667–17675. [[CrossRef](#)]
17. Zhang, H.; An, Z.; Li, F.; Tang, Q.; Lu, K.; Li, W. Synthesis and characterization of mesoporous c- ZrO_2 microspheres consisting of peanut-like nano-grains. *J. Alloy. Compd.* **2008**, *464*, 569–574. [[CrossRef](#)]
18. De La Rosa, E.; Diaz-Torres, L.; Salas, P.; Rodríguez, R. Visible light emission under UV and IR excitation of rare earth doped ZrO_2 nanophosphor. *Opt. Mater.* **2005**, *27*, 1320–1325. [[CrossRef](#)]
19. Almjasheva, O.; Garabadzhiu, A.; Kozina, Y.; Litvinchuk, L.; Dobritsa, V. Biological effect of zirconium dioxide-based nanoparticles. *Nanosyst. Phys. Chem. Math.* **2017**, *8*, 391–396. [[CrossRef](#)]
20. Li, P.; Chen, I.-W.; Penner-Hahn, J.E. X-ray-absorption studies of zirconia polymorphs. I. Characteristic local structures. *Phys. Rev. B.* **1993**, *48*, 10063–10073. [[CrossRef](#)]
21. Li, P.; Chen, I.-W.; Penner-Hahn, J.E. Effect of dopants on zirconia stabilization-An X-ray absorption study: I., Trivalent Dopants. *J. Am. Ceram. Soc.* **1994**, *77*, 118–128. [[CrossRef](#)]
22. Gupta, S.K.; Natarajan, V. Synthesis, characterization and photoluminescence spectroscopy of lanthanide ion doped oxide materials. *BARC Newsl.* **2015**, *46*, 14–21.
23. Tiseanu, C.; Parvulescu, V.I.; Avram, D.; Cojocaru, B.; Apostol, N.; Vela-Gonzalez, A.V.; Sanchez-Dominiguez, M. Structural, down- and phase selective up-conversion emission properties of mixed valent Pr doped into oxides with tetravalent cations. *Phys. Chem. Chem. Phys.* **2014**, *16*, 5793–5802. [[CrossRef](#)] [[PubMed](#)]
24. Hui, Y.; Zhao, S.; Xu, J.; Zhu, L.; Zhou, X.; Zou, B.; Wang, Y.; Cao, X. Doping concentration of Eu^{3+} as a fluorescence probe for phase transformation of zirconia. *J. Rare Earths* **2015**, *33*, 717–725. [[CrossRef](#)]
25. Marin, R.; Sponchia, G.; Zucchetta, E.; Riello, P.; Enrichi, F.; De Portu, G.; Benedetti, A. Monitoring the $t \rightarrow m$ martensitic phase transformation by photoluminescence emission in Eu^{3+} -doped zirconia powders. *J. Am. Ceram. Soc.* **2013**, *96*, 2628–2635. [[CrossRef](#)]

26. Tanner, P.A. Some misconceptions concerning the electronic spectra of tri-positive europium and cerium. *Chem. Soc. Rev.* **2013**, *42*, 5090–5101. [CrossRef] [PubMed]
27. Bünzli, J.-C.G.; Eliseeva, S.V. *Basics of Lanthanide Photophysics*; Springer Series on Fluorescence; Springer Science + Business Media, LLC: Berlin/Heidelberg, Germany, 2010; Volume 7, pp. 1–45. [CrossRef]
28. Tiseanu, C.; Cojocaru, B.; Parvulescu, V.I.; Sanchez-Dominiguez, M.; Primus, P.A.; Boutonnet, M. Order and disorder effects in nano-ZrO₂ investigated by micro-Raman and spectrally and temporarily resolved photoluminescence. *Phys. Chem. Chem. Phys.* **2012**, *14*, 12970. [CrossRef]
29. Bugrov, A.; Smyslov, R.Y.; Zavalova, A.; Kirilenko, D.A.; Pankin, D. Phase composition and photoluminescence correlations in nanocrystalline ZrO₂:Eu³⁺ phosphors synthesized under hydrothermal conditions. *Nanosyst. Phys. Chem. Math.* **2018**, *9*, 378–388. [CrossRef]
30. Meetei, S.D.; Singh, S.D. Effects of crystal size, structure and quenching on the photoluminescence emission intensity, lifetime and quantum yield of ZrO₂:Eu³⁺ nanocrystals. *J. Lumin.* **2014**, *147*, 328–335. [CrossRef]
31. Ahemen, I.; Dejene, F.B. Effect of Eu³⁺ ion concentration on phase transition, site symmetry and quantum efficiency of ZrO₂ nanocrystal rods. *J. Nanosci. Nanotechnol.* **2018**, *18*, 2429–2440. [CrossRef]
32. Quan, Z.; Wang, L.; Lin, J. Synthesis and characterization of spherical ZrO₂:Eu³⁺ phosphors by spray pyrolysis process. *Mater. Res. Bull.* **2005**, *40*, 810–820. [CrossRef]
33. Smits, K.; Grigorjeva, L.; Millers, D.; Sarakovskis, A.; Opalinska, A.; Fidelus, J.D.; Lojkowski, W. Europium doped zirconia luminescence. *Opt. Mater.* **2010**, *32*, 827–831. [CrossRef]
34. Tamrakar, R.K.; Bisen, D.; Upadhyay, K. Photoluminescence behavior of ZrO₂:Eu³⁺ with variable concentration of Eu³⁺ doped phosphor. *J. Radiat. Res. Appl. Sci.* **2015**, *8*, 11–16. [CrossRef]
35. Lovisa, L.X.; Andrés, J.; Gracia, L.; Li, M.S.; Paskocimas, C.A.; Bomio, M.R.D.; Araújo, V.D.; Longo, E.; Motta, F.V. Photoluminescent properties of ZrO₂:Tm³⁺, Tb³⁺, Eu³⁺ powders—A combined experimental and theoretical study. *J. Alloy. Compd.* **2017**, *695*, 3094–3103. [CrossRef]
36. Tiwari, N.; Kuraria, R.; Kuraria, S. Effect of variable trivalent europium concentration on photo- and thermoluminescence of zirconium dioxide nanophosphors. *Mater. Sci. Semicond. Process.* **2015**, *31*, 214–222. [CrossRef]
37. Bugrov, A.; Smyslov, R.Y.; Zavalova, A.; Kopitsa, G.P. The influence of chemical prehistory on the structure, photoluminescent properties, surface and biological characteristics of Zr_{0.98}Eu_{0.02}O_{1.99} nanophosphors. *Nanosyst. Phys. Chem. Math.* **2019**, *10*, 164–175. [CrossRef]
38. Colbea, C.; Avram, D.; Cojocaru, B.; Negrea, R.; Ghica, C.; Kessler, V.G.; Seisenbaeva, G.A.; Parvulescu, V.I.; Tiseanu, C. Full tetragonal phase stabilization in ZrO₂ nanoparticles using wet impregnation: Interplay of host structure, dopant concentration and sensitivity of characterization technique. *Nanomaterials* **2018**, *8*, 988. [CrossRef]
39. Wysokińska, E.; Cichos, J.; Zioło, E.; Bednarkiewicz, A.; Strządała, L.; Karbowski, M.; Hreniak, D.; Kałas, W. Cytotoxic interactions of bare and coated NaGdF₄:Yb³⁺:Er³⁺ nanoparticles with macrophage and fibroblast cells. *Toxicol. Vitro.* **2016**, *32*, 16–25. [CrossRef]
40. Lutterotti, L.; Matthies, S.; Wenk, H.; Schultz, A.S.; Richardson, J.W. Combined texture and structure analysis of deformed limestone from time-of-flight neutron diffraction spectra. *J. Appl. Phys.* **1997**, *81*, 594–600. [CrossRef]
41. Kirilenko, D.A.; Dideykin, A.; Aleksenskiy, A.; Sitnikova, A.; Konnikov, S.; Vul', A. One-step synthesis of a suspended ultrathin graphene oxide film: Application in transmission electron microscopy. *Micron* **2015**, *68*, 23–26. [CrossRef]
42. *Fibrosis Research*; Springer Science + Business Media, LLC: Berlin/Heidelberg, Germany, 2005; Volume 117, pp. 1–392.
43. Bugrov, A.; Zavalova, A.Y.; Smyslov, R.Y.; Anan'Eva, T.D.; Vlasova, E.N.; Mokeev, M.V.; Kryukov, A.E.; Kopitsa, G.P.; Pipich, V. Luminescence of Eu³⁺ ions in hybrid polymer-inorganic composites based on poly(methyl methacrylate) and zirconia nanoparticles. *Luminescence* **2018**, *33*, 837–849. [CrossRef] [PubMed]
44. De Mello, J.C.; Wittmann, H.F.; Friend, R.H. An improved experimental determination of external photoluminescence quantum efficiency. *Adv. Mater.* **1997**, *9*, 230–232. [CrossRef]
45. Vasilef, I. QtiPlot: Data Analysis and Scientific Visualization. Available online: <http://www.qtiplot.com/> (accessed on 15 November 2020).
46. Bersani, D.; Lottici, P.P.; Rangel, G.; Ramos, E.; Pecchi, G.; Gomez, R.; Lopez, T. Micro-Raman study of indium doped zirconia obtained by sol-gel. *J. Non-Crystalline Solids* **2004**, *345*, 116–119. [CrossRef]

47. Basahel, S.N.; Ali, T.T.; Mokhtar, M.; Narasimharao, K. Influence of crystal structure of nanosized ZrO₂ on photocatalytic degradation of methyl orange. *Nanoscale Res. Lett.* **2015**, *10*, 1–13. [[CrossRef](#)]
48. Gazzoli, D.; Mattei, G.; Valigi, M. Raman and X-ray investigations of the incorporation of Ca²⁺ and Cd²⁺ in the ZrO₂ structure. *J. Raman Spectrosc.* **2007**, *38*, 824–831. [[CrossRef](#)]
49. Kontoyannis, C.G.; Orkoulas, M. Quantitative determination of the cubic, tetragonal and monoclinic phases in partially stabilized zirconias by Raman spectroscopy. *J. Mater. Sci.* **1994**, *29*, 5316–5320. [[CrossRef](#)]
50. Guo, L.; Li, M.; Zhang, Y.; Ye, F. Improved toughness and thermal expansion of non-stoichiometry Gd_{2-x}Zr_{2+x}O_{7+x/2} ceramics for thermal barrier coating application. *J. Mater. Sci. Technol.* **2016**, *32*, 28–33. [[CrossRef](#)]
51. Bünzli, J.-C.G. On the design of highly luminescent lanthanide complexes. *Co-ord. Chem. Rev.* **2015**, 19–47. [[CrossRef](#)]
52. Yakimanskii, A.V.; Goikhman, M.Y.; Podeshvo, I.V.; Anan'Eva, T.D.; Nekrasova, T.N.; Smyslov, R.Y. Luminescence of Ln³⁺ lanthanide complexes in polymer matrices. *Polym. Sci. Ser. A* **2012**, *54*, 921–941. [[CrossRef](#)]
53. Chen, L.; Liu, Y.; Li, Y. Preparation and characterization of ZrO₂:Eu³⁺ phosphors. *J. Alloy. Compd.* **2004**, *381*, 266–271. [[CrossRef](#)]
54. Ebendorff-Heidepriem, H.; Ehrhart, D. Formation and UV absorption of cerium, europium and terbium ions in different valencies in glasses. *Opt. Mater.* **2000**, *15*, 7–25. [[CrossRef](#)]
55. Bugrov, A.; Smyslov, R.Y.; Anan'Eva, T.D.; Zavalova, A.; Kirilenko, D.A.; Almasheva, O. Soluble and insoluble polymer-inorganic systems based on poly(methyl methacrylate), modified with ZrO₂-LnO_{1.5} (Ln = Eu, Tb) nanoparticles: Comparison of their photoluminescence. *J. Lumin.* **2019**, *207*, 157–168. [[CrossRef](#)]
56. Prakasam, M.; Valsan, S.; Lu, Y.; Balima, F.; Lu, W.; Piticescu, R.; Largeteau, A. Nanostructured pure and doped zirconia: Synthesis and sintering for SOFC and optical applications. *Sinter. Technol. Method Appl.* **2018**, *2018*, 85–105.
57. Rainho, J.; Ananias, D.; Lin, Z.; Ferreira, A.; Carlos, L.D.; Rocha, J. Photoluminescence and local structure of Eu(III)-doped zirconium silicates. *J. Alloy. Compd.* **2004**, *374*, 185–189. [[CrossRef](#)]
58. Ishida, H.; Bünzli, J.-C.; Beeby, A. Guidelines for measurement of luminescence spectra and quantum yields of inorganic and organometallic compounds in solution and solid state (IUPAC Technical Report). *Pure Appl. Chem.* **2016**, *88*, 701–711. [[CrossRef](#)]
59. Kouva, S.; Honkala, K.; Lefferts, L.; Kanervo, J. Review: Monoclinic zirconia, its surface sites and their interaction with carbon monoxide. *Catal. Sci. Technol.* **2015**, *5*, 3473–3490. [[CrossRef](#)]
60. Tokiy, N.V.; Konstantinova, T.Y.; Savina, D.L.; Tokiy, V.V. Modeling of dehydration and dehydrogenation in pure and Ba-, Ca-, Sr- or Y-modified zirconia nanolayer. In *Hydrogen Materials Science and Chemistry of Carbon Nanomaterials*; Springer: Dordrecht, The Netherlands, 2004; Volume 172, pp. 291–298. [[CrossRef](#)]
61. Chen, B.-H.; Inbaraj, B.S. Various physicochemical and surface properties controlling the bioactivity of cerium oxide nanoparticles. *Crit. Rev. Biotechnol.* **2018**, *38*, 1003–1024. [[CrossRef](#)]
62. Nakamura, M.; Inuzuka, M.; Hashimoto, K.; Nagai, A.; Yamashita, K. Improving bioactivity and durability of yttria-stabilized zirconia. *J. Mater. Sci.* **2011**, *46*, 7335–7343. [[CrossRef](#)]
63. García-Moncada, N.; Bobadilla, L.F.; Poyato, R.; Lopez-Cartes, C.; Romero-Sarria, F.; Centeno, M.; Odriozola, J. A direct in situ observation of water-enhanced proton conductivity of Eu-doped ZrO₂: Effect on WGS reaction. *Appl. Catal. B Environ.* **2018**, *231*, 343–356. [[CrossRef](#)]
64. Patil, S.; Sandberg, A.; Heckert, E.; Self, W.; Seal, S. Protein adsorption and cellular uptake of cerium oxide nanoparticles as a function of zeta potential. *Biomaterials* **2007**, *28*, 4600–4607. [[CrossRef](#)] [[PubMed](#)]

Publisher's Note: MDPI stays neutral with regard to jurisdictional claims in published maps and institutional affiliations.



© 2020 by the authors. Licensee MDPI, Basel, Switzerland. This article is an open access article distributed under the terms and conditions of the Creative Commons Attribution (CC BY) license (<http://creativecommons.org/licenses/by/4.0/>).